Journal of Applied Physics

RESEARCH ARTICLE | MARCH 01 2023

Magnetization dynamics of a CoFe/Co_2MnSi magnetic bilayer structure

Special Collection: Recent Advances in Magnonics

Sujung Kim ; Yawen Guo ; Weigang Yang ; Toyanath Joshi; David Lederman ; Holger Schmidt

J. Appl. Phys. 133, 093902 (2023)
https://doi.org/10.1063/5.0128519

Journal of Applied Physics ARTICLE scitation.org/journal/jap

Magnetization dynamics of a CoFe/Co_2MnSi magnetic bilayer structure

Cite as: J. Appl. Phys. 133, 093902 (2023); doi: 10.1063/5.0128519
Submitted: 28 September 2022 · Accepted: 8 February 2023 ·
Published Online: 1 March 2023

Sujung Kim,[1] Yawen Guo,[1] Weigang Yang,[1] Toyanath Joshi,[2] David Lederman,[2] and Holger Schmidt[1,a)]

AFFILIATIONS

[1]Department of Electrical and Computer Engineering, University of California Santa Cruz, 1156 High Street, Santa Cruz, California 95064, USA
[2]Department of Physics, University of California Santa Cruz, 1156 High Street, Santa Cruz, California 95064, USA

Note: This paper is part of the Special Topic on Recent Advances in Magnonics.
[a)]**Author to whom correspondence should be addressed:** hschmidt@ucsc.edu

ABSTRACT

Half-metallic Heusler alloys are receiving significant attention for spintronic applications utilizing magnetic tunnel junctions and requiring large spin polarization. Co_2MnSi (CMS) is one of the most promising candidates for this purpose. Here, we report the magnetization dynamics of a thin, epitaxial CMS film in a magnetic CoFe/CMS bilayer structure sputtered on an MgO substrate. The magnetic precession frequency response of the CoFe/CMS bilayer shows a fourfold symmetry with respect to the azimuthal applied field angle, reflecting the crystal symmetry of the CMS layer and not the underlying CoFe film. Moreover, the effective Gilbert damping parameter exhibits inhomogeneous broadening at lower applied magnetic fields. At large fields, however, the azimuthal angle dependence disappears, and the intrinsic Gilbert damping is observed. This study provides insight into the dynamics of a magnetic bilayer structure that forms an integral element in spintronic applications.

I. INTRODUCTION

Epitaxially grown magnetic multilayers play a key role in spintronic devices,[1–3] where their layered structures are designed to provide precise control over the electronic and magnetic properties for applications such as magnetic random access memory (MRAM), sensors, and spin transistors. Many of these devices rely on multilayer magnetic tunnel junctions (MTJs),[1–12] in which high spin polarization is essential to maximize the tunnel magnetoresistance (TMR) and, thus, optimize device performance. Recently, Heusler alloys have received increasing attention for this purpose due to their half-metallic nature[13–18] and high Curie temperature,[19–21] and Co_2MnSi (CMS) has emerged as one of the most promising candidates.[22,23] CMS can crystallize in the ordered $L2_1$ crystal structure, which has been theoretically shown to possess nearly zero spin down density of states at the Fermi energy due to Slater–Pauli behavior,[24] and high spin polarization has been found in this phase.[25] By controlling the annealing temperature, CMS alloys can also crystallize in the $B2$ phase, which is half-metallic as well.[26] Indeed, excellent static behavior, including a TMR ratio of 570% at low temperature in a CMS/AlO/CMS structure[27] and 753% in a CMS/MgO/CoFe structure,[22] has been demonstrated. The crucially important interface quality between CMS and the tunneling oxide can be improved with a thin intermediate layer based on cobalt iron (e.g., CoFeB), resulting in TMR ratios as high as 222% at room temperature.[23] In addition to MTJ applications, Heusler alloys are also promising materials for spintronic THz emitters.[28,29] Moreover, multilayer structures with adjacent CoFe and CMS layers can also be used to build novel spintronic devices, such as THz sources based on nonlinear magnon–magnon interactions.[30]

It is, therefore, of great interest to investigate the magnetic properties of CMS in structures in which it is surrounded by another magnetic layer. In addition to static properties such as TMR, sound knowledge and understanding of the dynamic properties are also important as it determines the time-dependent device behavior and can reveal important material parameters such as the Gilbert damping parameter. Indeed, the suppression of spin-flip processes in half metals promises low damping,[31–33] and damping

values as low as $< 8 \times 10^{-4}$ have been reported in Co_2FeAl films[34] and Co_2MnSi films.[35]

Magnetization dynamics can be measured with different techniques. One of them is time-resolved magneto-optic Kerr effect (TR-MOKE) microscopy in which magnetic materials are non-invasively perturbed by a short laser pulse, and their dynamic response is analyzed with a second, delayed pulse.[36] Liu *et al.* have previously used this technique to analyze the magnetization dynamics of a thick (30 nm) CMS film grown with a non-magnetic Cr buffer layer on the MgO substrate and annealed at different temperatures.[37] They measured the precession frequency of the CMS film at low applied magnetic fields (below 1 kOe) and as a function of the azimuthal angle ϕ between the applied field and the [110] crystalline direction of the film. A fourfold symmetric dependence of both the precession frequency and damping as a function of ϕ was observed, caused by the magnetocrystalline anisotropy present in this cubic structure.

Here, we expand on these studies by investigating the magnetization dynamics of an epitaxial CMS layer that is part of an MgO/CoFe/CMS magnetic bilayer sequence that can act as a functional segment in future spintronic devices as discussed above. Using external magnetic fields applied at various polar and azimuthal angles, we extract the magnetization dynamics all the way up to the high-field limit where inhomogeneous broadening mechanisms disappear, and the intrinsic Gilbert damping of the material can be determined.[38] Additional comparison with the dynamics of a CoFe film reveals that the dynamic response remains determined by the geometry of the CMS crystal anisotropy and is not affected by the CoFe crystal geometry. We also find that the angular dependence of the damping parameter disappears in the high magnetic field limit.

II. SAMPLE PREPARATION AND EXPERIMENTAL PROCEDURE

Two different sample types were fabricated for this study. A reference sample consisting of a single, 10.8 nm thick CoFe film was prepared on an MgO [001] substrate [see Fig. 1(b)]. The MgO substrate was annealed at 800 °C at 100 Torr in an O_2 gaseous environment for 100 min, then the temperature was lowered to 700 °C, and the substrate was left in a vacuum. The substrate was then cooled down to 400 °C, and a thin layer of MgO was deposited by pulsed laser deposition (PLD) to improve the surface quality and to promote better crystallinity of the films. After the surface treatment, the substrate was transferred to an RF-Sputtering chamber while kept in a vacuum. A $Co_{50}Fe_{50}$ target was used to sputter a 10.8 nm thick CoFe film at room temperature, followed by annealing (500 °C for 30 min) and cooling (400 °C for 1 h) steps. The second

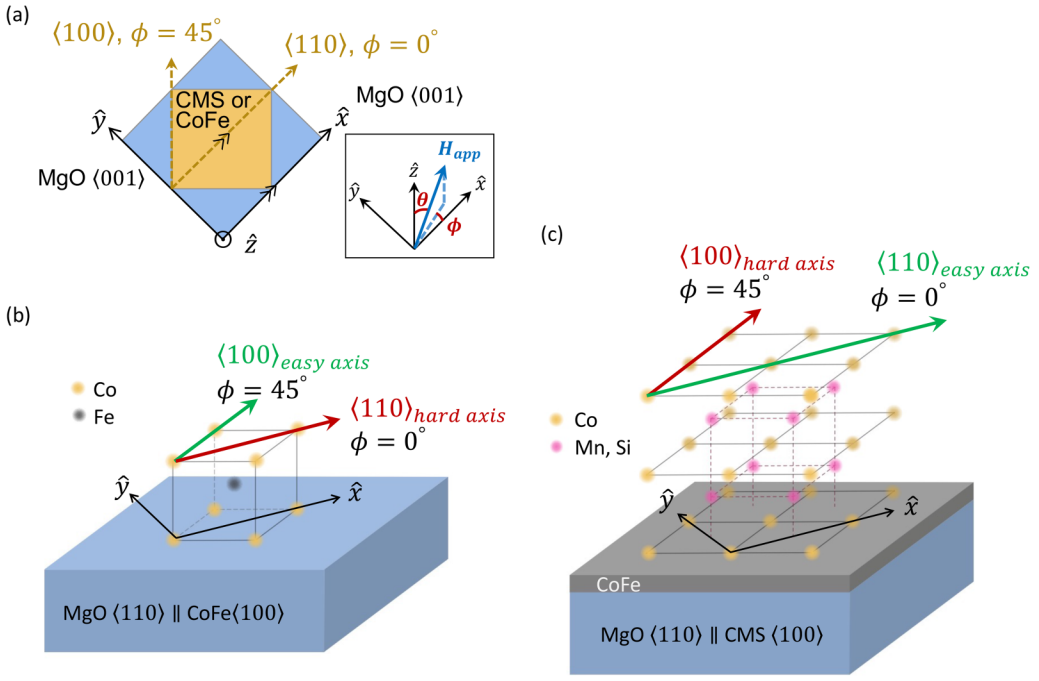

FIG. 1. Sample geometry. (a) Top–down view of CoFe and CMS ⟨110⟩directions are parallel to the MgO ⟨001⟩ direction and the *x*-axis. The inset shows the geometry of the applied magnetic field with respect to the Cartesian coordinate and the corresponding polar coordinate. (b) The unit cell of the magnetic single layer CoFe film on the MgO substrate. The magnetic easy axis (green arrow) of the CoFe film corresponds to the ⟨100⟩ direction and $\phi = 45^\circ$, and the magnetic hard axis (red arrow) of the CoFe film corresponds to the ⟨110⟩ direction and $\phi = 0^\circ$. (c) The unit cell of the CMS film grown on top of the CoFe film and the MgO substrate. The magnetic easy axis (green arrow) of the CMS film corresponds to the ⟨110⟩ direction and $\phi = 0^\circ$, and the magnetic hard axis (red arrow) of the CMS film corresponds to the ⟨100⟩ direction and $\phi = 45^\circ$.

sample consisted of a CoFe (1.7 nm)/CMS (7.0 nm) bilayer film [Fig. 1(c)]. The thin 1.7 nm CoFe film was prepared on a separate MgO [001] substrate using the same protocol. Additionally, an RF sputtering step to deposit a 7.0 nm CMS film at room temperature was performed, followed by annealing for 30 min at 400 °C.

X-ray diffraction experiments using a parallel-beam configuration, an incoming double-bounce Ge monochromator, and Cu Kα1 radiation ($\lambda = 0.154\,06$ nm) were used to study the bilayer sample's structure. The layer thickness parameters of the CoFe/CMS bilayer film were determined from x-ray reflectivity, confirming a thickness of 1.7 nm for the CoFe layer and 7.0 nm for the CMS layer with sharp interfaces of 0.3 nm roughness [Fig. 2(a)]. The epitaxial nature of the CMS was verified by taking pole figure scans of the CMS {202} peaks [Fig. 2(b)]. The pole figures show that the CMS [100] direction is indeed parallel to the MgO [110] direction, as depicted in Fig. 1.

High-angle x-ray diffraction scans about CMS (004) and CMS (022) revealed that the CMS layer was oriented along its [001] directions, as shown in the top graph of Fig. 2(c). The CMS (004) diffraction was composed of two peaks at $2\theta = 66.1°$ and $2\theta = 67.1°$, correspondingly labeled peak 1 and peak 2 in Fig. 2(c). The (022) reflection was also composed of two peaks, located at $2\theta = 44.7°$ and $2\theta = 45.88°$, labeled peak 2 and peak 1, respectively. We believe this is due to a sudden relaxation of the crystal structure as it grows, probably at a thickness smaller than 3.5 nm given the areas of the two peaks. Assuming that one of the

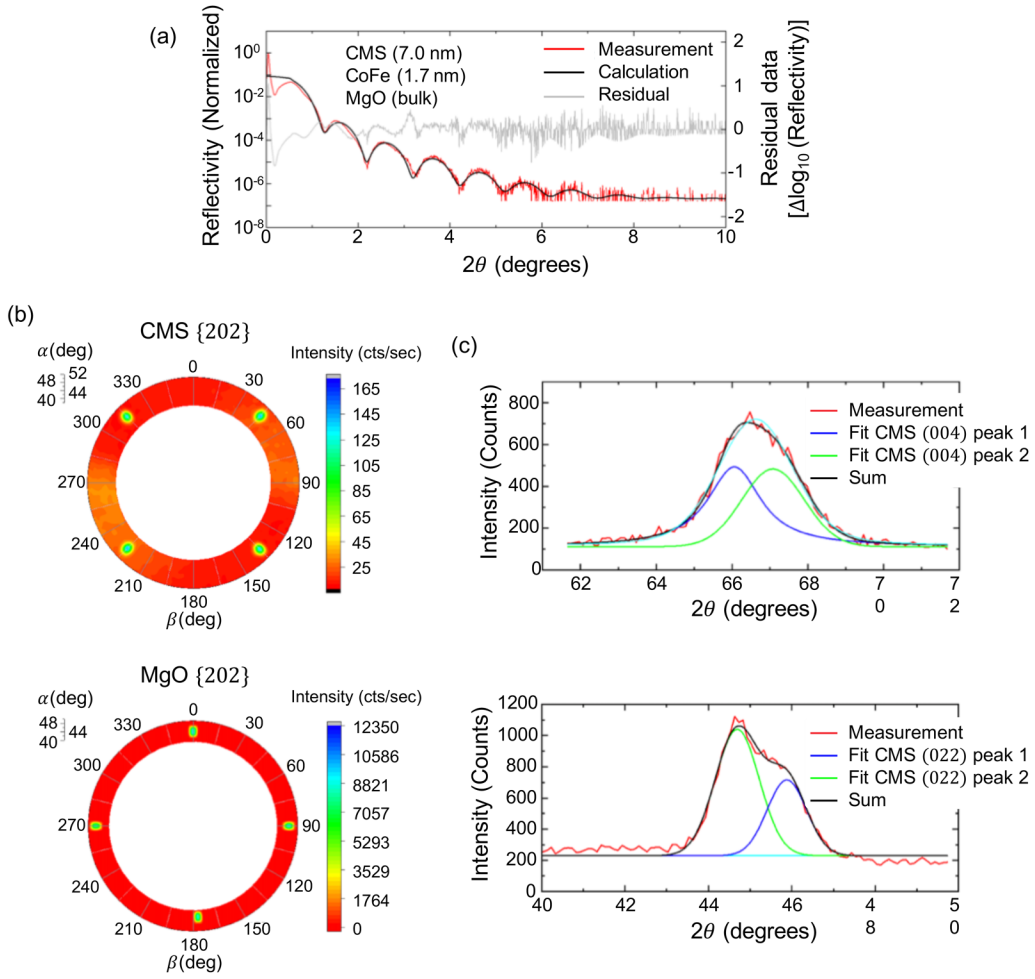

FIG. 2. X-ray analysis of the CoFe/CMS magnetic bilayer film. (a) X-ray reflectivity to measure the thickness of the CoFe/CMS layers. The red curve represents the measured data, while the black curve is a fit to an optical scattering model with 1.69 nm of CoFe, 6.95 nm of CMS, and 0.3 nm of interface roughness at each interface. The gray curve is the residual [$\log_{10}$ (measured data) − $\log_{10}$ (model calculation)]. (b) Pole figure of the CMS {202} peaks and the MgO substrate {202} peaks about the surface normal, corresponding to the MgO [001] direction, showing the alignment of the in-plane CMS [100] and the MgO [110] crystallographic directions. (c) Top: x-ray diffraction $\theta - 2\theta$ scan data (red) obtained with the scattering vector $\vec{q}$ along the direction perpendicular to the film's plane. Bottom: $\theta - 2\theta$ scan obtained with $\vec{q}$ along the CMS [022] direction with Gaussian lineshape fits. Gaussian peaks were fit to the data (green, blue), with the black curve being the sum of the two peaks.

crystals corresponds to peak 1 of the (004) reflection and peak 1 of the (022) reflection, we obtain a lattice constant out-of-plane equal to $d_{o,CMS1} = 0.565$ nm and an in-plane lattice constant of $d_{i,CMS1} = 0.553$ nm. For the crystal corresponding to peak 2, the lattice constant out-of-plane is $d_{o,CMS2} = 0.558$ nm, and the in-plane lattice constant is $d_{i,CMS2} = 0.591$ nm, with an uncertainty of ± 0.001 nm. The bulk CMS compound has a lattice constant of 0.5654 nm[39] and, therefore, it is likely that peak 1 of CMS (004) and CMS (022) corresponds to a relatively unstrained CMS layer, while peak 2 corresponds to a highly strained CMS layer. Indeed, the in-plane lattice constant corresponding to the in-plane (110) planes for the strained layer is $d_{i,CMS2}/\sqrt{2} = 0.418$ nm, which is close to the (001) lattice constant of MgO of 0.421 nm. In other words, initially, the film attempts to grow epitaxially with the MgO substrate (peak 2), causing a large amount of tensile strain (approximately 6%), and then releases its strain after less than 3.5 nm to obtain an almost cubic structure consistent with the bulk compound (peak 1). The CoFe seed layer plays a key role in achieving this epitaxy; CMS films grown directly on MgO were not epitaxial but grew with a preferential (110) orientation (data not shown). The CoFe layer in this sample is too thin to be measured with our x-ray apparatus, however.

Interestingly, a similar effect is found in the CoFe thin film. This film was capped with a thin layer of MgO to prevent oxidation. The x-ray analysis is shown in Fig. 3. The x-ray reflectivity shown in Fig. 3(a) indicated that the CoFe layer was 10.8 nm

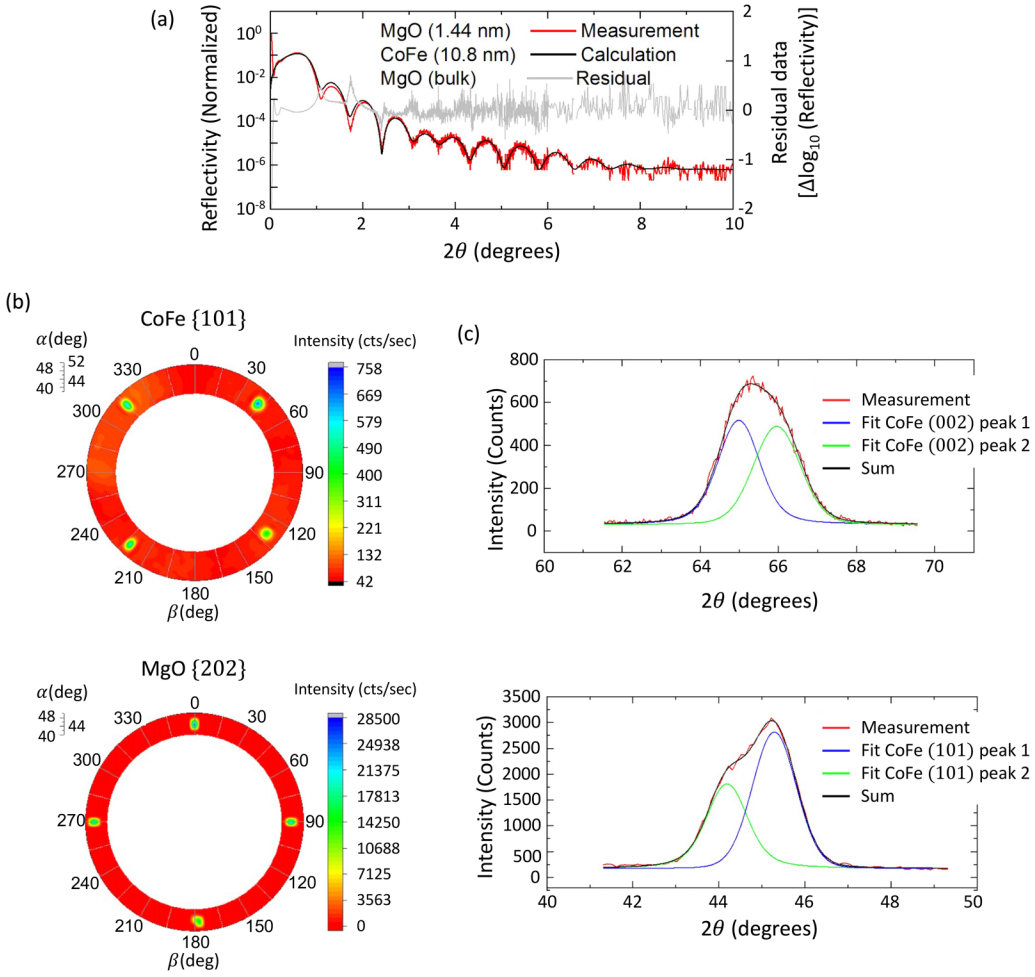

FIG. 3. X-ray analysis of the CoFe reference magnetic film. (a) X-ray reflectivity to measure the thickness of the CoFe layer. The red curve represents the measured data, while the black curve is a fit to an optical scattering model with 10.8 nm of CoFe and 1.4 nm of MgO capping layer, and 0.5 nm of interface roughness at each interface. The gray curve is the residual [$\log_{10}$ (measured data) – $\log_{10}$ (model calculation)]. (b) Pole figure of the CoFe {101} peaks and the MgO substrate {202} peaks about the surface normal, corresponding to the MgO [001] direction, showing the alignment of the in-plane CoFe [100] and the MgO [110] crystallographic directions. (c) Top: x-ray diffraction $\theta - 2\theta$ scan data (red) obtained with the scattering vector $\vec{q}$ along the direction perpendicular to the film's plane. Bottom: $\theta - 2\theta$ scan obtained with $\vec{q}$ along the CoFe [101] direction with Gaussian lineshape fits. Gaussian peaks were fit to the data (green, blue), with the black curve being the sum of the two peaks.

thick and that the MgO [110] axis is along the in-plane CoFe [100] axis, in agreement with the literature.[40] The pole figures shown in Fig. 3(b) confirm that the CoFe film is epitaxial with the in-plane CoFe [100] direction parallel to the MgO [110] direction. Figure 3(c) shows the high-angle x-ray scans of CoFe (002) and CoFe (101). Using the same analysis as the one described above for the CMS film, we obtain that the out-of-plane lattice constants for the crystal layer that corresponds to peak 1 are $d_{o,CoFe1} = 0.287$ nm and the in-plane lattice constant of $d_{i,CoFe1} = 0.279$ nm. For the second set of peaks (peak 2), we have out-of-plane lattice constant of $d_{o,CoFe2} = 0.283$ nm and in-plane lattice constant of $d_{i,CoFe2} = 0.297$ nm. The highly strained layer corresponding to peaks 2 results in an in-plane lattice constant of $d_{i,CoFe2}/\sqrt{2} = 0.420$ nm, also consistent with the epitaxial growth on MgO as described in Fig. 1.

There are two commonly observed phases in epitaxially grown CMS crystals—$L2_1$ and $B2$ phases—that are known to exhibit half-metallic behavior.[26] Unlike the $L2_1$ phase, where the Mn and Si atoms are highly ordered, Mn and Si atoms are randomly located at lattice points in the cubic unit cell in the $B2$ phase. To determine which phase of CMS was grown, we attempted to obtain pole figures and $\theta - 2\theta$ scans about the expected positions of the CMS (111) peak, but we were unable to find such a peak. Because the characteristic (111) peak of the $L2_1$ phase was not observed in the XRD scan, it is likely that the epitaxial CMS film possessed the $B2$ structure.

The magnetization dynamics of these samples were analyzed using a previously described[41] dual-color time-resolved magneto-optic Kerr effect (TR-MOKE) setup in polar Kerr geometry.[42] Briefly, an 800 nm femtosecond laser pulse (Coherent MIRA) was split into two beam paths. One of the beams was converted into a 400 nm pulse after passing through a second harmonic generator (SHG). This pump beam arrives at the sample plane, initiating the magnetic dynamics by delivering thermal energy. The probe beam path includes a motorized delay stage, which provides control over the time difference with which the two pulses arrive at the sample. Upon reflection at the surface of the magnetic film, the linearly polarized probe beam experiences Kerr rotation, and the reflected beam is detected with balanced photodetectors that collect the horizontal and vertical polarization components, respectively. As the pump beam is spectrally filtered after the reflection, the collected signals provide information on the change in polarization due to the magnetization dynamics.

III. RESULTS AND DISCUSSION

To establish a reference for the bilayer structure and to potentially separate the behavior of the CoFe layer from that of the CMS film, we first analyzed the magnetization dynamics of the epitaxially grown CoFe film. To this end, an external magnetic field of $H_{app} = 5$ kOe was applied at multiple polar angles (θ, angle with respect to the z-axis) and various azimuthal angles (ϕ, angle with respect to the x-axis in the x–y plane) [see the inset in Fig. 1(a)]. Specifically, polar angles of $\theta = 30^\circ$, 45°, and 55° were chosen and the azimuthal angle was scanned in each case between $0^\circ \leq \phi \leq 90^\circ$ to probe the full fourfold symmetry in the BCC structure. Figure 1(b) shows the unit cell of epitaxially grown CoFe on the MgO substrate. For CoFe grown on an MgO ⟨001⟩ substrate used in this study, the ⟨100⟩ easy axis coincides with the ⟨110⟩ direction of MgO as discussed earlier.

The time-dependent magnetization dynamics were extracted from the difference signal of the balanced photodetectors and recorded via LabVIEW software (Fig. 4). After the subtraction of an exponentially decaying thermal background, the Kerr rotation (θ_k), which is proportional to the magnetization change in the z direction, was fit to the equation

$$\theta_k = A \sin(\omega t + \varphi) e^{-t/\tau} \tag{1}$$

to extract the magnetic precession frequency and the effective damping parameter.[43,44] Here, $\omega = 2\pi f$ is the angular precession frequency described by the Landau–Lifshitz–Gilbert (LLG) equation, and $\alpha_{eff} = 1/\omega\tau$ is the effective Gilbert damping parameter.

Figure 5(a) shows the dependence of the magnetization precession frequency as a function of azimuthal angles for each of the three different polar angles. The frequency response depends strongly on ϕ and is symmetrically distributed around $\phi = 45^\circ$, reflecting the fourfold symmetry character of the BCC crystal structure that originates from the magnetocrystalline anisotropy. At $\phi = 0^\circ$ and 90°, the projection of the magnetic field in the x–y plane is applied along the magnetic hard axis [⟨110⟩, Fig. 1(b)], and the lowest frequency was observed. At $\phi = 45^\circ$, the in-plane component of the magnetic field is applied along the magnetic easy axis [⟨100⟩ orientation, Fig. 1(b)], and the highest precession frequency was observed. The magnetic field was also applied and scanned including the face diagonal ($\theta = 45^\circ$, $\phi = 45^\circ$) and body diagonal ($\theta = 55^\circ$, $\phi = 0^\circ, 90^\circ$) directions of the CoFe structure.

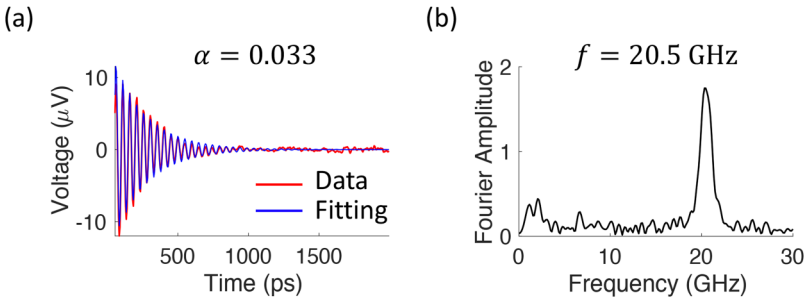

FIG. 4. (a) Time trace and (b) its Fourier transformed data of a magnetic single layer CoFe thin film to illustrate the data analysis. The time trace data were taken at $H_{app} = 5$ kOe, $\theta = 30^\circ$, $\phi = 45^\circ$.

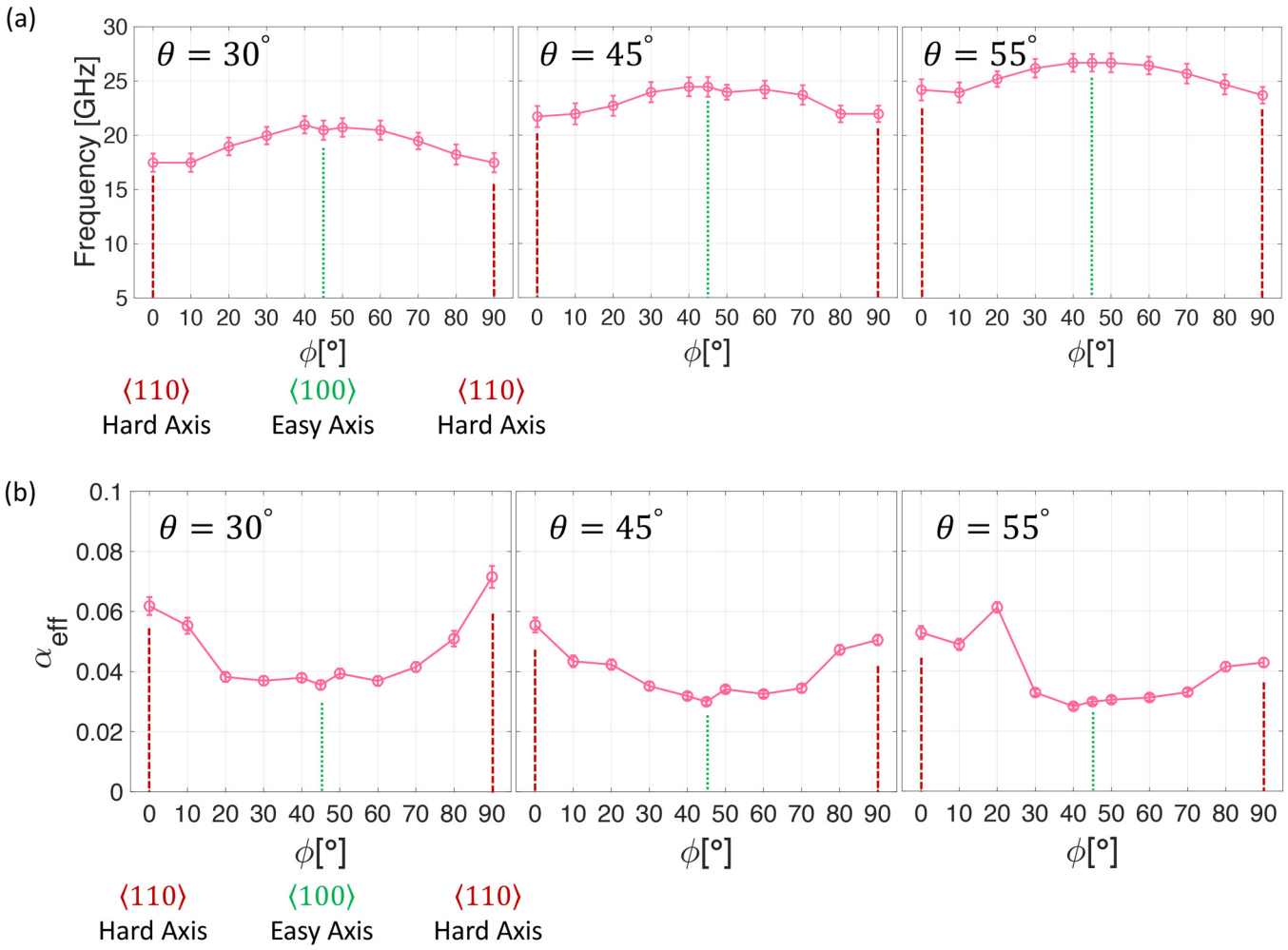

FIG. 5. (a) Precession frequency and (b) effective damping parameter of a single magnetic CoFe film at various applied magnetic fields. The data were taken at a constant magnetic field (5 kOe) applied at three polar angles ($\theta = 30^\circ$, 45°, and 55° from left to right), while sweeping the azimuthal angles from $\phi = 0^\circ$ to 90° to probe the full fourfold symmetry of the cubic crystal. The red dashed (green dotted) lines are guides to the eye to denote when the in-plane component of the applied magnetic field is along the magnetic hard (easy) axis.

Qualitatively similar frequency responses were consistently observed for all applied polar angles. Next, the damping was extracted from the same time data trace used for the frequency analysis for the same range of applied magnetic fields [Fig. 5(b)]. Again, the fourfold symmetry corresponding to the magnetocrystalline anisotropy was also observed in the effective damping parameter. However, the effective damping parameter was highest when the in-plane component of the magnetic field was applied along the hard axis ($\phi = 0^\circ, 90^\circ$) and lowest when the in-plane component of the magnetic field was applied along the easy axis ($\phi = 45^\circ$).

After having established the dynamic behavior of a single CoFe layer, we investigated the magnetization dynamics in view of the CoFe/CMS crystalline structure. Figures 6(a)–6(c) show the field scans of the frequency response of the CoFe/CMS bilayer for the three different polar angles. As in Fig. 4(b), each plot in the figure corresponds to 17 applied field values ranging from 1 to 5 kOe in 0.25 kOe steps. As in the case of the single layer CoFe film, the frequency response was symmetrically centered around at $\phi = 45^\circ$ [Fig. 6(d), shown for three representative applied field values], representing the magnetocrystalline anisotropy of the fourfold symmetry character exhibited in cubic crystals. In sharp contrast to the CoFe measurements, however, the azimuthal scan now shows a frequency maximum when the in-plane component of the magnetic field was applied along the ⟨110⟩ direction and a minimum along the ⟨100⟩ direction. This is because the epitaxially grown CMS film has the ⟨110⟩ direction as a magnetic easy axis [Fig. 1(c)], and the ⟨100⟩ direction corresponds to the magnetic hard axis [Fig. 1(c)]. This confirms that the dynamic magnetic behavior of the CMS film is not altered by the presence of the thin CoFe layer.

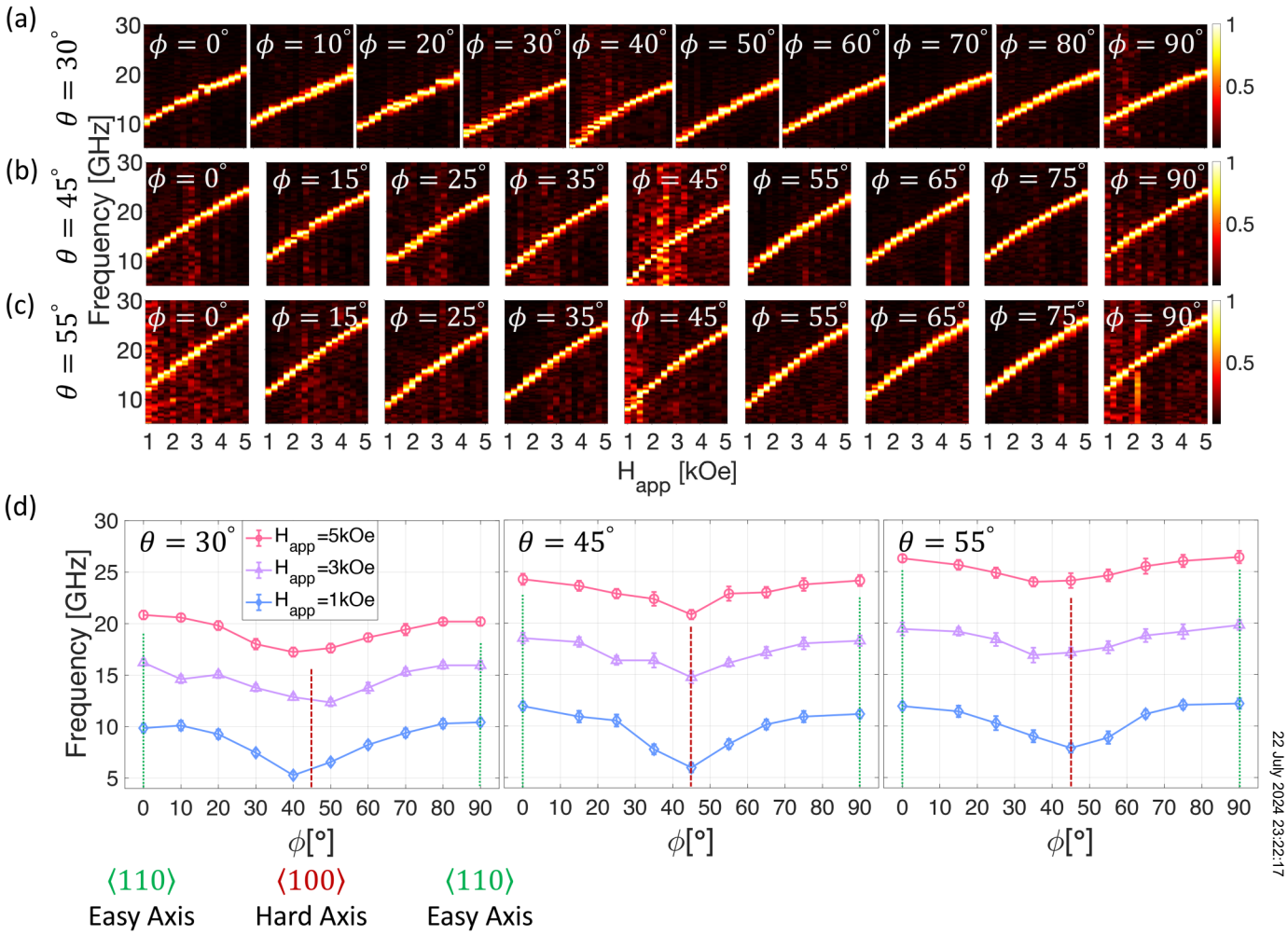

FIG. 6. (a)–(c) Frequency response of the CoFe/CMS magnetic bilayer at various applied magnetic fields. The magnetic field was applied at three polar angles θ = (a) 30°, (b) 45°, and (c) 55°, and various azimuthal angles from $\phi = 0^{\circ}$ to 90° (left to right) while sweeping the intensity of applied magnetic field from 1 to 5 kOe. (d) Frequency response of [(a)–(c)] taken at $H_{app} = 1$, 3, and 5 kOe. The green dotted (red dashed) lines are guides to the eye to denote when the in-plane component of the applied magnetic field is along the magnetic easy (hard) axis.

Next, the field-dependent effective damping parameter was extracted by fitting the same data sets to Eq. (1), and the results are displayed for all the applied field intensities ranging from 1 to 5 kOe. The field dependence of α_{eff} is plotted in Fig. 7(a) for various representative azimuthal angles and for all three polar angles. For all parameter sets, we observe the characteristic decrease of the effective damping as the applied field increases and inhomogeneous broadening mechanisms are eliminated.[38]

Generally, the effective lifetime τ of the magnetization precession is given by

$$\frac{1}{\tau} = \frac{1}{\tau_{Gilb}} + \frac{1}{\tau_{ext}}, \tag{2}$$

where τ_{Gilb} describes the intrinsic Gilbert damping and τ_{ext} represents extrinsic damping mechanisms that reduce τ (and, thus, increase α_{eff}) and typically depend on H_{app}. In our CMS film, two-magnon scattering (TMS), e.g., due to strain-induced anisotropy inhomogeneities, is a dominant source of extrinsic damping.[45] Qualitatively identical curves to Fig. 7(a) have been analyzed with models that account for TMS[46,47] showing excellent agreement with the data (see Ref. 38).

In addition, at low fields, we see an apparent difference in α_{eff} as the azimuthal angle is varied while the high-field limit appears uniform for all orientations. To extract this field dependence more clearly, we show the dependence of α_{eff} on azimuthal orientation in Fig. 7(b) for low, intermediate, and high applied fields for comparison. Indeed, at low fields, we find a clear dependence of α_{eff} on ϕ with maximum damping at $\phi = 45^{\circ}$, in agreement with the observations of Liu *et al.*,[37] where the inhomogeneous broadening

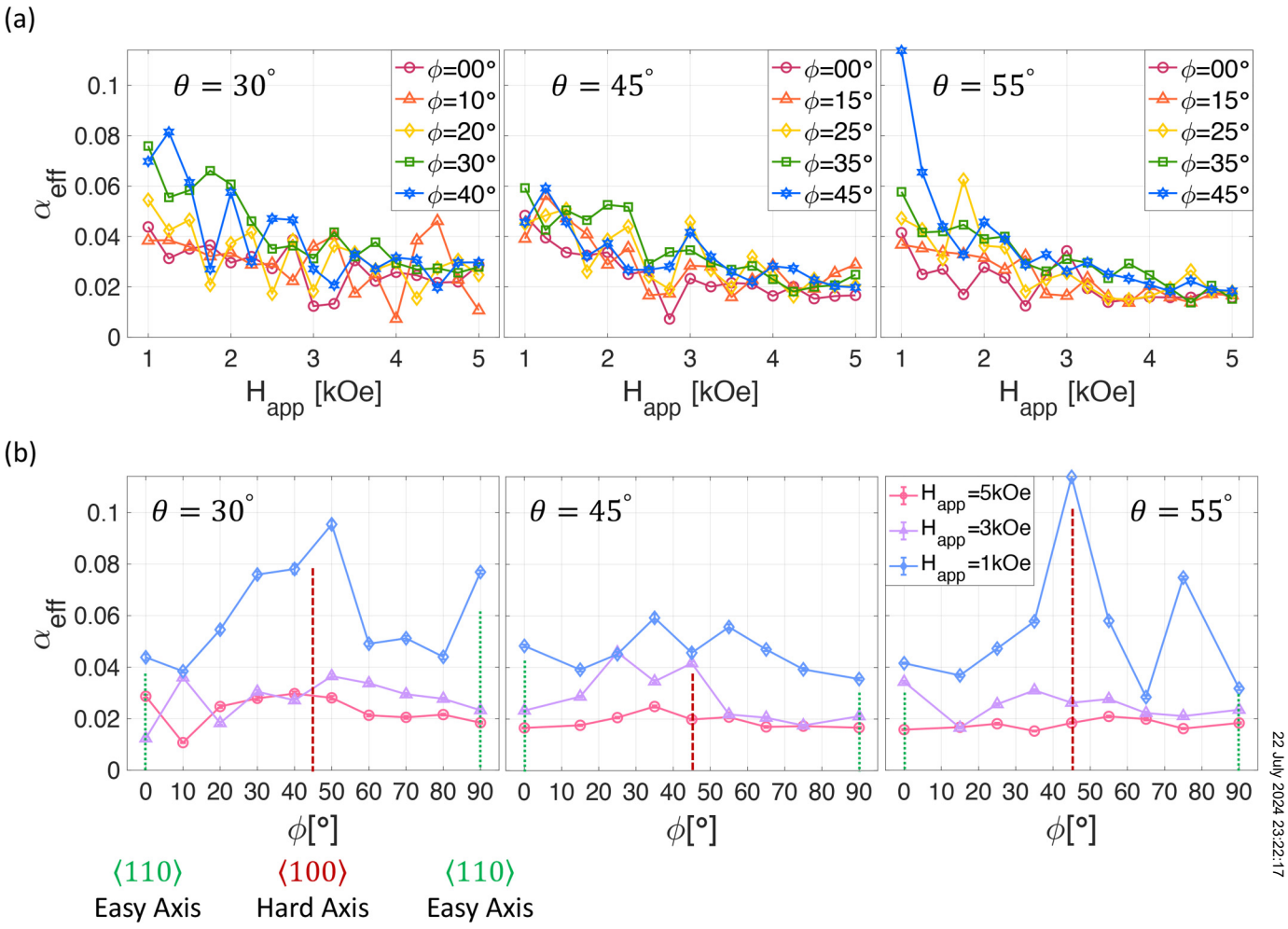

FIG. 7. Effective magnetic damping parameter of the CoFe/CMS magnetic bilayer film taken from the same data set as in Fig. 5. (a) The data were taken when the magnetic field was applied from 1 to 5 kOe, at three polar angles ($\theta = 30°$, 45°, and 55°, from left to right) and various azimuthal angles from $\phi = 0^{\circ}$ to 90°. Again, the green dotted (red dashed) lines are guides to the eye to denote when the in-plane component of the applied magnetic field is along the magnetic easy (hard) axis. (b) Effective damping parameter as a function of the azimuthal angle at representative three applied fields for comparison, showing a strong orientational dependence at low fields and convergence to the intrinsic Gilbert damping at high fields due to the elimination of inhomogeneous broadening.

explains the magnetocrystalline anisotropy. At high applied fields, however, this dependence disappears and the intrinsic Gilbert damping of ~0.02 is observed for all parameter combinations. We note that the relatively high α_{eff} may be due to the mechanical strains present in both the very thin CoFe and the CMS films. Such strain creates defects in the crystal when the strain is released, which cause additional spin wave scattering, leading to a larger effective damping parameter.

IV. CONCLUSION

In summary, we investigated the magnetization dynamics of an epitaxial CMS thin film in a magnetic bilayer structure. Specifically, the dependence of the dynamic parameters on the polar and azimuthal orientation of an applied magnetic field with respect to the MgO substrate was carefully analyzed. We found that the frequency of optically induced magnetization precessions in the CMS layer is fully determined by the magnetocrystalline anisotropy of the CMS structure and not perturbed by the diametrically opposite behavior of an adjacent thin CoFe film. In addition, field and angle dependent analysis of the precession damping revealed that variations reflecting the crystal symmetry and anisotropy are only observed at low applied fields (~1 kOe), while at high fields, the effective damping converges to the intrinsic Gilbert damping for all experimental configurations.

These results reveal the magnetic dynamics of CMS layers embedded in a larger functional, magnetic bilayer structure, thus providing guidance for the design of future spintronic devices for

which further reduction of the Gilbert damping is possible by optimizing the sample structure.

ACKNOWLEDGMENTS

The authors thank C. Washburn and B. Sharif for fruitful discussions. Part of this work was supported by a gift from Magtera, Inc.

AUTHOR DECLARATIONS

Conflict of Interest

The authors have no conflicts to disclose.

Author Contributions

Sujung Kim: Conceptualization (equal); Data curation (equal); Formal analysis (equal); Investigation (equal); Methodology (equal); Software (equal); Validation (equal); Visualization (equal); Writing – original draft (equal). **Yawen Guo:** Data curation (equal); Investigation (equal); Software (equal); Visualization (equal); Writing – review & editing (equal). **Weigang Yang:** Data curation (equal); Investigation (equal). **Toyanath Joshi:** Data curation (equal); Investigation (equal). **David Lederman:** Data curation (equal); Formal analysis (equal); Investigation (equal); Resources (equal); Validation (equal); Visualization (equal); Writing – review & editing (equal). **Holger Schmidt:** Conceptualization (equal); Formal analysis (equal); Funding acquisition (equal); Methodology (equal); Project administration (equal); Resources (equal); Supervision (equal); Validation (equal); Writing – original draft (equal); Writing – review & editing (equal).

DATA AVAILABILITY

The data that support the findings of this study are available from the corresponding author upon reasonable request.

REFERENCES

[1]S. S. P. Parkin, C. Kaiser, A. Panchula, P. M. Rice, B. Hughes, M. Samant, and S. Yang, Nat. Mater. **3**, 862 (2004).
[2]M. Yamamoto, T. Marukame, T. Ishikawa, K. Matsuda, T. Uemura, and M. Arita, J. Phys. D: Appl. Phys. **39**, 824 (2006).
[3]Y. Liu, A. N. Chiaramonti, D. K. Schreiber, H. Yang, S. S. P. Parkin, O. G. Heinonen, and A. K. Petford-Long, Phys. Rev. B **83**, 165413 (2011).
[4]D. D. Djayaprawira, K. Tsunekawa, M. Nagai, H. Maehara, S. Yamagata, and N. Watanabe, Appl. Phys. Lett. **86**, 092502 (2005).
[5]Y. Nagamine, H. Maehara, K. Tsunekawa, D. D. Djayaprawira, and N. Watanabe, Appl. Phys. Lett. **89**, 162507 (2006).
[6]J. C. A. Huang, C. Y. Hsu, W. H. Chen, Y. H. Lee, S. F. Chen, C. P. Liu, and Y. Tzeng, J. Appl. Phys. **104**, 073909 (2008).
[7]W. Wang, H. Sukegawa, R. Shan, S. Mitani, and K. Inomata, Appl. Phys. Lett. **95**, 182502 (2009).
[8]W. Wang, E. Liu, M. Kodzuka, H. Sukegawa, M. Wojcik, E. Jedryka, G. H. Wu, K. Inomata, S. Mitani, and K. Hono, Phys. Rev. B **81**, 140402(R) (2010).
[9]S. Ikeda, K. Miura, H. Yamamoto, K. Mizunuma, H. D. Gan, M. Endo, S. Kanai, J. Hayakawa, F. Matsukura, and H. Ohno, Nat. Mater. **9**, 721 (2010).
[10]J. Zhang, C. Franz, M. Czerner, and C. Heiliger, Phys. Rev. B **90**, 184409 (2014).
[11]Z. Wen, H. Sukegawa, T. Furubayashi, J. Koo, K. Inomata, S. Mitani, J. P. Hadorn, T. Ohkubo, and K. Hono, Adv. Mater. **26**, 6483 (2014).
[12]A. P. Chen, J. D. Burton, E. Y. Tsymbal, Y. P. Feng, and J. Chen, Phys. Rev. B **98**, 045129 (2018).
[13]I. Galanakis, J. Phys.: Condens. Matter **14**, 6329 (2002).
[14]S. Picozzi, A. Continenza, and A. J. Freeman, Phys. Rev. B **66**, 094421 (2002).
[15]S. Wurmehl, G. H. Fecher, K. Kroth, F. Kronast, H. A. Dürr, Y. Takeda, Y. Saitoh, K. Kobayashi, H. Lin, G. Schönhense, and C. Felser, J. Phys. D: Appl. Phys. **39**, 803 (2006).
[16]I. Galanakis and P. Mavropoulos, J. Phys.: Condens. Matter **19**, 315213 (2007).
[17]M. Jourdan, J. Minár, J. Braun, A. Kronenberg, S. Chadov, B. Balke, A. Gloskovskii, M. Kolbe, H. J. Elmers, G. Schönhense, H. Ebert, C. Felser, and M. Kläui, Nat. Commun. **5**, 3974 (2014).
[18]S. Andrieu, A. Neggache, T. Hauet, T. Devolder, A. Hallal, M. Chshiev, A. M. Bataille, P. Le Fèvre, and F. Bertran, Phys. Rev. B **93**, 094417 (2016).
[19]P. J. Webster, J. Phys. Chem. Solids **32**, 1221 (1971).
[20]J. Kübler, A. R. William, and C. B. Sommers, Phys. Rev. B **28**, 1745 (1983).
[21]E. Şaşıoğlu, L. M. Sandratskii, and P. Bruno, Phys. Rev. B **72**, 184415 (2005).
[22]S. Tsunegi, Y. Sakuraba, M. Oogane, K. Takanashi, and Y. Ando, Appl. Phys. Lett. **93**, 112506 (2008).
[23]S. Tsunegi, Y. Sakuraba, M. Oogane, H. Naganuma, K. Takanashi, and Y. Ando, Appl. Phys. Lett. **94**, 252503 (2009).
[24]I. Galanakis and P. H. Dederichs, Phys. Rev. B **66**, 174429 (2002).
[25]Y. Sakuraba, J. Nakata, M. Oogane, H. Kubota, Y. Ando, A. Sakuma, and T. Miyazaki, Jpn. J. Appl. Phys. **44**, L1100 (2005).
[26]Y. Kota and A. Sakuma, J. Phys.: Conf. Ser. **266**, 012094 (2011).
[27]Y. Sakuraba, M. Hattori, M. Oogane, Y. Ando, H. Kato, A. Sakuma, T. Miyazaki, and H. Kubota, Appl. Phys. Lett. **88**, 192508 (2006).
[28]G. Bierhance, A. Markou, O. Gueckstock, R. Rouzegar, Y. Behovits, A. L. Chekhov, M. Wolf, T. S. Seifert, C. Felser, and T. Kampfrath, Appl. Phys. Lett. **120**, 082401 (2022).
[29]R. Gupta, S. Husain, A. Kumar, R. Brucas, A. Rydberg, and P. Svedlindh, Adv. Opt. Mater. **9**, 2001987 (2021).
[30]B. G. Tankhilevich and Y. Korenblit, J. Phys. Conf. Ser. **263**, 012004 (2011).
[31]S. Mizukami, D. Watanabe, M. Oogane, Y. Ando, Y. Miura, M. Shirai, and T. Miyazaki, J. Appl. Phys. **105**, 07D306 (2009).
[32]L. Bainsla, R. Yilgin, M. Tsujikawa, K. Z. Suzuki, M. Shirai, and S. Mizukami, J. Phys. D: Appl. Phys. **51**, 495001 (2018).
[33]C. Guillemard, S. Petit-Watelot, J.-C. Rojas-Sánchez, J. Hohlfeld, J. Ghanbaja, A. Bataille, P. Le Fèvre, F. Bertran, and S. Andrieu, Appl. Phys. Lett. **115**, 172401 (2019).
[34]W. K. Peria, T. A. Peterson, A. P. McFadden, T. Qu, C. Liu, C. J. Palmstrøm, and P. A. Crowell, Phys. Rev. B **101**, 134430 (2020).
[35]C. de Melo, C. Guillemarda, A. M. Friedela, V. Palina, J. C. Rojas-Sáncheza, S. Petit-Watelota, and S. Andrieua, Appl. Mater. Today **25**, 101174 (2021).
[36]B. Koopmans, "Laser-induced magnetization dynamics," in *Spin Dynamics in Confined Magnetic Structures II* (Springer, Berlin, 2003), pp. 256–323.
[37]Y. Liu, L. R. Shelford, V. V. Kruglyak, R. J. Hicken, Y. Sakuraba, M. Oogane, and Y. Ando, Phys. Rev. B **81**, 094402 (2010).
[38]W. G. Yang, M. Jaris, D. L. Hibbard-Lubow, C. Berk, and H. Schmidt, Phys. Rev. B **97**, 224410 (2018).
[39]S. Fujii, S. Ishida, and S. Asano, J. Phys. Soc. Jpn. **63**, 1881 (1994).
[40]Y. Li, F. Zeng, S. S.-L. Zhang, H. Shin, H. Saglam, V. Karakas, O. Ozatay, J. E. Pearson, O. G. Heinonen, Y. Wu, A. Hoffmann, and W. Zhang, Phys. Rev. Lett. **122**, 117203 (2019).
[41]C. Berk, M. Jaris, W. Yang, S. Dhuey, S. Cabrini, and H. Schmidt, Nat. Commun. **10**, 2652 (2019).
[42]S. Kim, Nat. Rev. Phys. **4**, 288 (2022).

[43]T. Rasing, H. van den Berg, T. Gerrits, and J. Hohlfeld, "Ultrafast magnetization and switching dynamics," in *Spin Dynamics in Confined Magnetic Structures II* (Springer, Berlin, 2003), pp. 216–255.
[44]C. G. Malinowski, K. C. Kuiper, R. Lavrijsen, H. J. M. Swagten, and B. Koopmans, Appl. Phys. Lett. **94**, 102501 (2009).
[45]J. Dubowik, K. Załęski, H. Głowiński, and I. Gościańska, Phys. Rev. B **84**, 184438 (2011).
[46]A. Capua, S. Yang, T. Phung, and S. S. P. Parkin, Phys. Rev. B **92**, 224402 (2015).
[47]S. Iihama, A. Sakuma, H. Naganuma, M. Oogane, S. Mizukami, and Y. Ando, Phys. Rev. B **94**, 174425 (2016).